INTERNATIONAL JOURNAL FOR NUMERICAL METHODS IN ENGINEERING, VOL. 38, 3591–3610 (1995)

THE LEAST-SQUARES FINITE ELEMENT METHOD FOR LOW-MACH-NUMBER COMPRESSIBLE VISCOUS FLOWS

SHENG-TAO YU

NYMA SETAR Team, NASA Lewis Research Center, Brook Park, OH 44142, U.S.A.

BO-NAN JIANG

Institute for Computational Mechanics and Propulsion, OAI, NASA Lewis Research Center, Cleveland, OH, U.S.A.

NAN-SUEY LIU

NASA Lewis Research Center, Cleveland, OH, U.S.A.

AND

JIE WU

Institute for Computational Mechanics and Propulsion, OAI, NASA Lewis Research Center, Cleveland, OH, U.S.A.

SUMMARY

The present paper reports the development of the Least-Squares Finite Element Method (LSFEM) for simulating compressible viscous flows at low Mach numbers in which the incompressible flows pose as an extreme. The conventional approach requires special treatments for low-speed flows calculations: finite difference and finite volume methods are based on the use of the staggered grid or the preconditioning technique, and finite element methods rely on the mixed method and the operator-splitting method. In this paper, however, we show that such a difficulty does not exist for the LSFEM and no special treatment is needed. The LSFEM always leads to a symmetric, positive-definite matrix through which the compressible flow equations can be effectively solved. Two numerical examples are included to demonstrate the method: driven cavity flows at various Reynolds numbers and buoyancy-driven flows with significant density variation. Both examples are calculated by using full compressible flow equations.

KEY WORDS: low-Mach-number flows; LSFEM

INTRODUCTION

In this paper, low-Mach-number, compressible, viscous flows are of interest. Low-speed flows with significant temperature variations are compressible due to the density variation induced by heat addition. For example, a significant heat addition occurs in combustion-related flow fields. Inside a chemical vapour deposition reactor, strong heat radiation also results in significant density variation. Although the flow speed is slow, one must employ the compressible flow equations to simulate such flows. However, it is well known that the conventional methods, which can handle high-speed compressible flows easily, fail miserably when applied to these low-Mach-number flows.

In the past, because of wide applications of the low-Mach-number flows, the issue of the efficiency and robustness of the calculations has been investigated. Most of the research, however,

CCC 0029–5981/95/213591–20

Received 5 July 1994

Revised 13 December 1994

utilizes the finite difference and finite volume methods; few attempts have been made using the finite element methods. Conventional finite difference and finite volume methods in solving low-Mach-number flows can be divided into two categories: the pressure-based methods and the density-based methods. The pressure-based methods have their root in the SIMPLE-type algorithm.[1] Essentially, a staggered grid has to be employed, i.e. the pressure and velocities are stored at different nodes. In addition, one usually has to employ a pressure correction equation (or another derived equation) instead of the original continuity equation when solving the equation set. This approach, to some extent, is similar to the Galerkin mixed finite element methods[2] for incompressible Navier–Stokes equations. In the Galerkin mixed method, different elements have to be used to interpolate the velocity and the pressure in order to satisfy the LBB condition[2] for the existence and stability of the discrete solution. Moreover, this approach results in an asymmetric, non-positive-definite coefficient matrix which cannot be effectively solved by using iterative methods.

On the other hand, the density-based methods use the same nodes for the velocities and the pressure. Merkle *et al.*[3,4] have successfully developed several density-based methods for both low-Mach-number flows and all-speed flows. Theoretical discussion can be found in Turkel's work.[5] These methods are an extension of the computational schemes for high-speed, compressible flows. All these aerodynamic codes were designed based on the hyperbolic characteristic of the Euler equations; the viscous terms were assumed effective only in a small portion of the domain and were interpreted as the damping of the numerical waves. When simulating low-Mach-number flows, however, the flow field is no longer dominated by the inviscid flow. The conventional aerodynamic codes encounter insurmountable slow-down. As a result, various treatments have been developed to enhance the efficiency. These treatments stem from preconditioning the Jacobian matrices of the convective terms in the flow equations to improve their condition numbers. Usually, two steps are involved. First, according to Chorin,[6] one adds a time derivative of pressure together with a multiplicative variable β, i.e. the pseudo-compressibility term, to the continuity equation. As a result, numerically viable time derivative terms exist in every equation even for flows at the low-speed (incompressible) limit. Consequently, based on the inviscid terms of the flow equations, the resultant equations become hyperbolic, and a numerical method for a hyperbolic system can be employed to advance the system in time.

Since the transient solution is not of interest, one can enhance the computational efficiency by tuning up the propagation speed and damping effect of numerical waves so that the calculation can reach steady state faster. This is done by premultiplying a preconditioning matrix to the equation set. The eigenvalues of the convective-term Jacobian matrices are scaled to the same order of magnitude. Therefore, the stability of numerical waves is ensured and the time marching process is under control.

However, it is obvious that when low-Mach-number flows are of interest, the viscous terms play an important role and the flow system is elliptic. When using the preconditioning technique, one fabricates an artificial hyperbolic system in order to employ a time marching scheme to advance the system to a steady state. In other words, the preconditioning method is based on conditioning the inviscid part of the governing equations—one can find very limited discussion for treatment of the viscous terms. It is not clear how one can apply the method to the low-speed extreme such as Stokes flows.

In the finite element methods, fewer attempts have been carried out on calculating low-Mach-number flows. For flow fields inside chemical vapour deposition reactors, Einset and Jensen[7] developed a low-Mach-number formulation which was then solved by Galerkin mixed method. In developing the low-Mach-number formulation, Einsted *et al.* proposed a correlation between the density and temperature based on the low-speed condition. The density in the governing equations was then replaced by the temperature. The equation set was solved by a mixed method which results in an asymmetric, non-positive-definite coefficient matrix. Einsted *et al.* inverted the matrix by the Conjugate Gradient Squared (CGS) method and the Generalized Minimal Residual (GMRES) method. Hafez *et al.*[26] proposed a unified approach for numerical simulations of Navier–Stokes equations. In their work, the choice of the variables and the non-dimensionalization strategy were carefully designed so that the formulation is valid for both compressible and incompressible flows with heat transfer. The equations were then solved by a partial least-squares procedure with artificial dissipation introduced into the system of equations. However, the numerical method results in an asymmetric, non-positive-definite coefficient matrix. Therefore, more work is needed to make the method applicable to large-scale calculations. Previously, Lefebvre *et al.*[24,25] used the LSFEM for simulating compressible and incompressible flows. They have tried both linear and quadratic, triangular elements and successfully simulated the flows with strong shocks.

Because the low-Mach-number flows are closely related to the incompressible flows, it may be worthwhile to briefly review other treatments developed for the incompressible flows. In the finite difference setting, Chorin[8] proposed to use a fractional step procedure to solve the incompressible flow equations. Later on, it was pointed out by Schneider *et al.*[9] and Kawahara *et al.*[10] that, by using the fractional step procedure, the restrictions imposed by the LBB condition for mixed formulation no longer apply. Various finite element schemes based on this procedure have been successfully developed and applied to incompressible flows using equal-order interpolation.[11–14] Other approaches, such as the Galerkin least-squares method proposed by Hughes *et al.*[15] and Sampaio,[16] were shown to have similar effects. A wider interpretation of such schemes was described by Zienkiewicz and Wu.[13] In addition, the fractional step procedure has been extended by Zienkiewicz and Wu to high-speed compressible Navier–Stokes equations[17] and shallow water equations.[18]

In this paper, a set of first-order equations is proposed for the low-Mach-number flows, in which the unknowns include variables such as the vorticity, the pressure variation and the divergence of velocity. With proper non-dimensionalization, the magnitude of each term in the governing equations, which depends on the Mach number of the flow field, can be clearly discerned. As a result, a set of equations suitable for low-Mach-number flows is derived.

We employ the LSFEM as the numerical scheme to solve the low-Mach-number flows. This approach is an extension of the LSFEM for incompressible flows which has been developed by Jiang *et al.*[19–21] The LSFEM always leads to a symmetric, positive-definite matrix which can be efficiently inverted by an iterative scheme such as the conjugate gradient method. In the present paper, however, a direct solver is employed because the formulation and the feasibility of the LSFEM for low-Mach-number flows are of interest instead of the computational efficiency.

In the next section, we present the governing equations to be solved by the LSFEM. In order to use simple C^0 elements, we convert the second-order transport equations to first-order ones by introducing new variables into the equations. Then, the system of equations is non-dimensionalized for low-Mach-number flows. In Section 3, the implementation of LSFEM is elaborated in detail. The temporal derivative terms of the flow equations are discretized by the Euler implicit method. Although the transient solution is not of interest, the temporal derivative terms serve as a relaxation scheme for marching towards a steady state. The non-linear terms are linearized by Newton's method. The discrete equations are formulated in an increment form which is then solved by the LSFEM. In the last section, two numerical examples are presented: driven cavity flows at various Reynolds numbers and buoyancy-driven flows at various Rayleigh numbers. Both cases are calculated by using the compressible flow formulation.

2. THEORETICAL MODELLING

2.1. *Two-dimensional compressible Navier–Stokes equations*

In the present work, two-dimensional, compressible, viscous flow equations are of concern:

$$\frac{\partial \rho}{\partial t} + u\frac{\partial \rho}{\partial x} + v\frac{\partial \rho}{\partial y} + \rho\left(\frac{\partial u}{\partial x} + \frac{\partial v}{\partial y}\right) = 0 \tag{1}$$

$$\rho\frac{\partial u}{\partial t} + \rho u\frac{\partial u}{\partial x} + \rho v\frac{\partial u}{\partial y} + \frac{\partial p}{\partial x}$$

$$= \mu\frac{\partial}{\partial x}\left[2\frac{\partial u}{\partial x} - \frac{2}{3}\left(\frac{\partial u}{\partial x} + \frac{\partial v}{\partial y}\right)\right] + \mu\frac{\partial}{\partial y}\left(\frac{\partial u}{\partial y} + \frac{\partial v}{\partial x}\right) \tag{2}$$

$$\rho\frac{\partial v}{\partial t} + \rho u\frac{\partial v}{\partial x} + \rho v\frac{\partial v}{\partial y} + \frac{\partial p}{\partial y}$$

$$= \mu\frac{\partial}{\partial y}\left[2\frac{\partial v}{\partial y} - \frac{2}{3}\left(\frac{\partial u}{\partial x} + \frac{\partial v}{\partial y}\right)\right] + \mu\frac{\partial}{\partial x}\left(\frac{\partial u}{\partial y} + \frac{\partial v}{\partial x}\right) - \rho g \tag{3}$$

$$\rho C_p\frac{\partial T}{\partial t} + \rho C_p u\frac{\partial T}{\partial x} + \rho C_p v\frac{\partial T}{\partial y} - \left(\frac{\partial p}{\partial t} + u\frac{\partial p}{\partial x} + v\frac{\partial p}{\partial y}\right)$$

$$= \Phi + k\left(\frac{\partial^2 T}{\partial x^2} + \frac{\partial^2 T}{\partial y^2}\right) - \rho g v \tag{4}$$

$$\Phi = 2\mu\left[\left(\frac{\partial u}{\partial x}\right)^2 + \left(\frac{\partial v}{\partial y}\right)^2 \frac{1}{2}\left(\frac{\partial u}{\partial y} + \frac{\partial v}{\partial x}\right)^2\right] - \frac{2}{3}\mu\left(\frac{\partial u}{\partial x} + \frac{\partial v}{\partial y}\right)^2 \tag{5}$$

where ρ is the density, u and v are the velocities in the respective directions, T is the temperature and Φ is the viscous dissipation. Physical properties such as the viscosity μ, the conductivity k and the constant pressure specific heat C_p are assumed constant throughout the flow field. Note that the co-ordinate system is chosen so that the gravity is in the negative y direction. Equation (1) is the continuity equation; equations (2) and (3), the momentum equations; and equation (4), the energy equation.

To solve the second-order transport equations, the least-squares method requires the use of undesirable C^1 (derivative continuous) elements. In order to employ C^0 elements, we introduce new variables into the flow system, including the divergence of velocity, the vorticity and the heat conduction fluxes. As a result, a set of first-order equations is obtained:

$$\frac{\partial \rho}{\partial t} + u\frac{\partial \rho}{\partial x} + v\frac{\partial \rho}{\partial y} + \rho\theta = 0 \tag{6}$$

$$\rho\frac{\partial u}{\partial t} + \rho u\frac{\partial u}{\partial x} + \rho v\frac{\partial u}{\partial y} + \frac{\partial p}{\partial x} = \mu\left(\frac{4}{3}\frac{\partial \theta}{\partial x} - \frac{\partial \omega}{\partial y}\right) \tag{7}$$

$$\rho\frac{\partial v}{\partial t} + \rho u\frac{\partial v}{\partial x} + \rho v\frac{\partial v}{\partial y} + \frac{\partial p}{\partial y} = \mu\left(\frac{4}{3}\frac{\partial \theta}{\partial y} + \frac{\partial \omega}{\partial x}\right) - \rho g \tag{8}$$

$$\rho C_p \frac{\partial T}{\partial t} + \rho C_p u \frac{\partial T}{\partial x} + \rho C_p v \frac{\partial T}{\partial y} - \left(\frac{\partial p}{\partial t} + u \frac{\partial p}{\partial x} + v \frac{\partial p}{\partial y} \right)$$
$$= \mu \left[\frac{4}{3}\theta^2 + \omega^2 + 4\left(\frac{\partial u}{\partial y}\frac{\partial v}{\partial x} - \frac{\partial u}{\partial x}\frac{\partial v}{\partial y} \right) \right] + \frac{\partial q_x}{\partial x} + \frac{\partial q_y}{\partial y} - \rho g v \tag{9}$$

where the variable θ is the divergence of the flow velocity, ω is the vorticity and q_x and q_y are the heat conduction fluxes in the respective directions. They are defined as

$$\theta = \frac{\partial u}{\partial x} + \frac{\partial u}{\partial x} \tag{10}$$

$$\omega = \frac{\partial v}{\partial x} - \frac{\partial u}{\partial y} \tag{11}$$

$$q_x = k\frac{\partial T}{\partial x} \tag{12}$$

$$q_y = k\frac{\partial T}{\partial y} \tag{13}$$

In addition to the above equations, we also need a constraint for the heat conduction fluxes that satisfies the alternative rule of partial differentiation:

$$\frac{\partial q_x}{\partial y} - \frac{\partial q_y}{\partial x} = 0 \tag{14}$$

The above governing equations, equations (6)–(14), are closed by the equation of state,

$$p = \rho R T \tag{15}$$

where R is the gas constant. Note that equation (15) is an algebraic correlation between thermodynamic properties of the fluid flow. This correlation could be enforced by replacing the density in the transport equations by a combination of temperature and pressure as was done by Einset and Jensen.[7] In this paper, however, we weakly impose the equation of state at each grid node. We shall illustrate the treatment in the following section.

2.2. Non-dimensionalization

To proceed, the governing equations, equations (6)–(15), are non-dimensionalized by appropriate parameters:

$$\rho^* = \frac{\rho}{\rho_\infty}, \quad u^* = \frac{u}{U_\infty}, \quad v^* = \frac{v}{U_\infty}$$
$$\theta^* = \frac{\theta L}{U_\infty}, \quad \omega^* = \frac{\omega L}{U_\infty}, \quad p'^* = \frac{p'}{\rho_\infty U_\infty^2}$$
$$T^* = \frac{T}{T_\infty}, \quad x^* = \frac{x}{L}, \quad y^* = \frac{y}{L}$$

where ρ_∞, U_∞, T_∞ and L are reference values of density, velocity, temperature and a length scale. Note that special care is taken in non-dimensionalizing the derivatives of pressure. Since we are interested in the low-speed flows, the pressure distribution is rather uniform. Therefore, we consider the pressure profile is composed of small variations p' imposed on a uniform background, such as $p = \bar{p} + p'$. The background pressure $\bar{p}$ then can be dropped out in the spatial and temporal derivatives. The pressure variation p' exists due to the flow velocities and, thus, is non-dimensionalized by a reference kinetic energy $\rho_\infty U_\infty^2$. This treatment is similar to that for incompressible flows. Therefore, as a rule of thumb, the formulation proposed here is applicable for $M \leqslant 0{\cdot}3$, in which $M = 0{\cdot}3$ is the conventional lower bound for the compressible effect starting to be effective due to the flow speed.

The non-dimensionalized system of equations can be expressed as

$$\frac{\partial \rho}{\partial t} + u\frac{\partial \rho}{\partial x} + v\frac{\partial \rho}{\partial y} + \rho\theta = 0 \tag{16}$$

$$\rho\frac{\partial u}{\partial t} + \rho u\frac{\partial u}{\partial x} + \rho v\frac{\partial u}{\partial y} + \frac{\partial p'}{\partial x} = \frac{1}{Re}\left(\frac{4}{3}\frac{\partial \theta}{\partial x} - \frac{\partial \omega}{\partial y}\right) \tag{17}$$

$$\rho\frac{\partial v}{\partial t} + \rho u\frac{\partial v}{\partial x} + \rho v\frac{\partial v}{\partial y} + \frac{\partial p'}{\partial y} = \frac{1}{Re}\left(\frac{4}{3}\frac{\partial \theta}{\partial y} + \frac{\partial \omega}{\partial x}\right) - \frac{1}{2\varepsilon Fr}\rho \tag{18}$$

$$\begin{aligned}\rho\frac{\partial T}{\partial t} + \rho u\frac{\partial T}{\partial x} + \rho v\frac{\partial T}{\partial y} - (\gamma - 1)M^2\left(\frac{\partial p'}{\partial x} + u\frac{\partial p'}{\partial x} + v\frac{\partial p'}{\partial y}\right)\\ = \frac{(\gamma-1)M^2}{Re}\left[\frac{4}{3}\theta^2 + \omega^2 + 4\left(\frac{\partial u}{\partial y}\frac{\partial v}{\partial x} - \frac{\partial u}{\partial x}\frac{\partial v}{\partial y}\right)\right]\\ + \frac{\partial q_x}{\partial x} + \frac{\partial q_y}{\partial y} - \frac{(\gamma-1)M^2}{2\varepsilon Fr}\rho v\end{aligned} \tag{19}$$

$$\theta = \frac{\partial u}{\partial x} + \frac{\partial v}{\partial y} \tag{20}$$

$$\omega = \frac{\partial v}{\partial x} - \frac{\partial u}{\partial y} \tag{21}$$

$$q_x = \frac{1}{Pe}\frac{\partial T}{\partial x} \tag{22}$$

$$q_y = \frac{1}{Pe}\frac{\partial T}{\partial y} \tag{23}$$

$$\frac{\partial q_x}{\partial y} - \frac{\partial q_y}{\partial x} = 0 \tag{24}$$

Note that the superscript * is neglected in the equation set for convenience. The dimensionless numbers in the equations are defined as

$$M = \frac{U_\infty}{\sqrt{\gamma R T_\infty}}, \quad Fr = \frac{U_\infty^2}{2\varepsilon g L}, \quad Ra = \frac{2\varepsilon g L^3}{\nu\alpha}$$

$$Pr = \frac{\nu}{\alpha}, \quad Re = \sqrt{\frac{RaFr}{Pr}}, \quad Pe = RePr$$

$$\alpha = \frac{k}{\rho C_p}, \quad \gamma = \frac{C_p}{C_v}$$

where M is the Mach number, Fr, the Froude number, Ra, the Rayleigh number, Pr, the Prandtl number, Re, the Reynolds number, Pe, the Peclet number, α, the thermal diffusivity, and γ, the ratio of specific heats. The temperature difference parameter ε is defined as

$$\varepsilon = \frac{\Delta T}{2T_\infty} = \frac{T_h - T_c}{T_h + T_c} \tag{25}$$

where T_h and T_c are the specified hot and cold temperatures in a thermal convection problem. Note that, for low-Mach-number flows ($M \ll 1$), the pressure derivative terms, the viscous dissipation terms, and the buoyancy term in the energy equation, equation (19), become negligible. In addition, the non-dimensionalized equation of state is imposed to close the equation set,

$$1 + \gamma M^2 p' = \rho T \tag{26}$$

For $M \ll 1$, the density and temperature become reciprocals of each other which is similar to that proposed by Einset and Jensen[7] and Hafez *et al.*[26]

3. THE LEAST-SQUARES FINITE ELEMENT METHOD

3.1. The first-order system

The first-order system of equations, equations (16)–(24), can be cast into a vector form,

$$\mathbf{A}'_0 \frac{\partial \mathbf{q}}{\partial t} + \mathbf{A}'_1 \frac{\partial \mathbf{q}}{\partial x} + \mathbf{A}'_2 \frac{\partial \mathbf{q}}{\partial y} + \mathbf{S}' = 0 \tag{27}$$

where $\mathbf{q} = (\rho, u, v, T, \theta, \omega, q_x, q_y, p')^{\mathrm{T}}$. To proceed, the time derivative term in equation (27) is discretized by the Euler implicit method, which leads to a first-order accuracy in time. In addition, the discretized time marching term is formulated in a delta form: $\mathbf{A}_0'^n(\Delta\mathbf{q}/\Delta t)$, where $\Delta\mathbf{q} = \mathbf{q}^{n+1} - \mathbf{q}^n$, and the superscript n denotes the previous time step. The non-linear terms of the governing equations, including the convection and source terms, are then linearized by Newton's method in the following fashion:

$$\left(\mathbf{A}'_1(q)\frac{\partial \mathbf{q}}{\partial x}\right)^{n+1} = \mathbf{A}_1'^n \frac{\partial \mathbf{q}^n}{\partial x} + \mathbf{A}_1'^n \frac{\partial \Delta\mathbf{q}^n}{\partial x} + \frac{\partial \mathbf{A}_1'^n}{\partial \mathbf{q}} \Delta\mathbf{q} \frac{\partial \mathbf{q}^n}{\partial x}$$

$$\mathbf{S}'^{n+1} = \mathbf{S}'^n + \left(\frac{\partial \mathbf{S}}{\partial \mathbf{q}}\right)'^n \Delta\mathbf{q} \tag{28}$$

Note that the same treatment is also applied to the non-linear terms differentiated with respect to y.

After manipulation, we obtain a new set of equations in vector form ready for finite element discretization,

$$\mathbf{A}_0^n \Delta\mathbf{q} + \mathbf{A}_1^n \frac{\partial \Delta\mathbf{q}}{\partial x} + \mathbf{A}_1^n \frac{\partial \mathbf{q}^n}{\partial x} + \mathbf{A}_2^n \frac{\partial \Delta\mathbf{q}}{\partial y} + \mathbf{A}_2^n \frac{\partial \mathbf{q}^n}{\partial y} + \mathbf{S}^n = 0 \tag{29}$$

Note that the coefficient matrices $\mathbf{A}_0, \mathbf{A}_1$ and $\mathbf{A}_2$ in equation (29) are different from those in equation (27) due to linearization by Newton's method, and we distinguish them by dropping the $'$. The coefficient matrix for the time marching term $\mathbf{A}_0$ can be expressed as

$$\mathbf{A}_0 = \begin{bmatrix} 1+\Delta t\theta & \dfrac{\partial \rho}{\partial x}\Delta t & \dfrac{\partial \rho}{\partial y}\Delta t & 0 & \rho\Delta t & 0 & 0 & 0 & 0 \\ \left(u\dfrac{\partial u}{\partial x}+v\dfrac{\partial u}{\partial y}\right)\Delta t & \rho\left(1+\dfrac{\partial u}{\partial x}\right)\Delta t & \rho\dfrac{\partial u}{\partial y}\Delta t & 0 & 0 & 0 & 0 & 0 & 0 \\ \left(u\dfrac{\partial v}{\partial x}+v\dfrac{\partial v}{\partial y}\right)\Delta t & \rho\dfrac{\partial v}{\partial x}\Delta t & \rho\left(1+\dfrac{\partial v}{\partial y}\right)\Delta t & 0 & 0 & 0 & 0 & 0 & 0 \\ \left(u\dfrac{\partial T}{\partial x}+v\dfrac{\partial T}{\partial y}\right)\Delta t & \left(\rho\dfrac{\partial T}{\partial x}-(\gamma-1)M^2\dfrac{\partial p'}{\partial x}\right)\Delta t & \left(\rho\dfrac{\partial T}{\partial y}-(\gamma-1)M^2\dfrac{\partial p'}{\partial y}\right)\Delta t & \rho & -\dfrac{8(\gamma-1)M^2}{3Re}\theta\Delta t & -\dfrac{2(\gamma-1)M^2}{Re}\omega\Delta t & 0 & 0 & -(\gamma-1)M^2 \\ 0 & 0 & 0 & 0 & 1 & 0 & 0 & 0 & 0 \\ 0 & 0 & 0 & 0 & 0 & 1 & 0 & 0 & 0 \\ 0 & 0 & 0 & 0 & 0 & 0 & 1 & 0 & 0 \\ 0 & 0 & 0 & 0 & 0 & 0 & 0 & 1 & 0 \\ 0 & 0 & 0 & 0 & 0 & 0 & 0 & 0 & 0 \end{bmatrix} \tag{30}$$

The coefficient matrices $\mathbf{A}_1$ and $\mathbf{A}_2$ for spatial derivatives are given as

$$\mathbf{A}_1 = \begin{bmatrix} u\Delta t & 0 & 0 & 0 & 0 & 0 & 0 & 0 & 0 \\ 0 & \rho u\Delta t & 0 & 0 & -\frac{4}{3}\frac{1}{Re}\Delta t & 0 & 0 & 0 & \Delta t \\ 0 & 0 & \rho u\Delta t & 0 & 0 & -\frac{1}{Re}\Delta t & 0 & 0 & 0 \\ 0 & \frac{4(\gamma-1)M^2}{Re}\frac{\partial v}{\partial y}\Delta t & -\frac{4(\gamma-1)M^2}{Re}\frac{\partial u}{\partial y}\Delta t & \rho u\Delta t & 0 & 0 & -\Delta t & 0 & -(\gamma-1)M^2 u\Delta t \\ 0 & -1 & 0 & 0 & 0 & 0 & 0 & 0 & 0 \\ 0 & 0 & -1 & 0 & 0 & 0 & 0 & 0 & 0 \\ 0 & 0 & 0 & -\frac{1}{Pe} & 0 & 0 & 0 & 0 & 0 \\ 0 & 0 & 0 & 0 & 0 & 0 & 0 & 0 & 0 \\ 0 & 0 & 0 & 0 & 0 & 0 & 0 & -1 & 0 \end{bmatrix} \tag{31}$$

$$\mathbf{A}_2 = \begin{bmatrix} v\Delta t & 0 & 0 & 0 & 0 & 0 & 0 & 0 & 0 \\ 0 & \rho v\Delta t & 0 & 0 & 0 & -\frac{1}{Re}\Delta t & 0 & 0 & 0 \\ 0 & 0 & \rho v\Delta t & 0 & -\frac{4}{3Re}\Delta t & 0 & 0 & 0 & \Delta t \\ 0 & -\frac{4(\gamma-1)M^2}{Re}\frac{\partial v}{\partial x}\Delta t & \frac{4(\gamma-1)M^2}{Re}\frac{\partial u}{\partial x}\Delta t & \rho v\Delta t & 0 & 0 & 0 & -\Delta t & -(\gamma-1)M^2 v\Delta t \\ 0 & 0 & -1 & 0 & 0 & 0 & 0 & 0 & 0 \\ 0 & 1 & 0 & 0 & 0 & 0 & 0 & 0 & 0 \\ 0 & 0 & 0 & 0 & 0 & 0 & 0 & 0 & 0 \\ 0 & 0 & 0 & -\frac{1}{Pe} & 0 & 0 & 0 & 0 & 0 \\ 0 & 0 & 0 & 0 & 0 & 0 & 1 & 0 & 0 \end{bmatrix} \tag{32}$$

The source vector is

$$\mathbf{S} = (0, 0, \rho/(2\varepsilon Fr), \rho v(\gamma-1)M^2/(2\varepsilon Fr), 0, 0, 0, 0, 0)^{\mathrm{T}} \tag{33}$$

As mentioned above, we are interested in the steady-state solution. Here, the time derivative terms are purposely included in the transport equations for two numerical advantages. First, the employment of the time marching method can enhance the convergence rate by providing a flexible control of Δt to maintain a uniform CFL number over the computational domain. Second, we use the increment of flow properties $\Delta\mathbf{q}$ over each time step as the dependent variable so that the final converged, steady-state solution is independent of both the initial condition and the numerical convergence history. This practice is rather commonplace in finite difference/volume methods, and it poses no problem for application to the finite element method.

3.2. *Least-squares method and discretization*

For convenience, we rewrite the governing equations in the following operator form:

$$\mathbf{L}\Delta\mathbf{q} = \mathbf{f} \tag{34}$$

where the linear operator $\mathbf{L}$ is defined as

$$\mathbf{L} = \mathbf{A}_0^n + \mathbf{A}_1^n \frac{\partial}{\partial x} + \mathbf{A}_2^n \frac{\partial}{\partial y} \tag{35}$$

The right-hand-side vector is

$$\mathbf{f} = -\mathbf{A}_1^n \frac{\partial \mathbf{q}^n}{\partial x} - \mathbf{A}_2^n \frac{\partial \mathbf{q}^n}{\partial y} - \mathbf{S}^n \tag{36}$$

To proceed, we define the least-squares functional of the residual $\mathbf{R} = \mathbf{L}\Delta\mathbf{q} - \mathbf{f}$ for admissible $\Delta\mathbf{q}$ as

$$J(\Delta\mathbf{q}) = \int_\Omega \mathbf{R}^{\mathrm{T}} \cdot \mathbf{R}\, \mathrm{d}\Omega \tag{37}$$

Minimizing the least-squares functional $J(\Delta\mathbf{q})$ with respect to $\Delta\mathbf{q}$ leads to

$$\delta J(\Delta\mathbf{q}) = 0 \tag{38}$$

That is,

$$\int_\Omega (\mathbf{L}\delta\Delta\mathbf{q})^{\mathrm{T}} \cdot (\mathbf{L}\Delta\mathbf{q} - \mathbf{f})\, \mathrm{d}\Omega = 0 \tag{39}$$

where δ denotes the variation of the function. Let $\delta\Delta\mathbf{q} = \mathbf{v}$, and equation (39) can be written as

$$\int_\Omega (\mathbf{L}\mathbf{v})^{\mathrm{T}}(\mathbf{L}\Delta\mathbf{q})\, \mathrm{d}\Omega = \int_\Omega (\mathbf{L}\mathbf{v})^{\mathrm{T}} \mathbf{f}\, \mathrm{d}\Omega \tag{40}$$

To employ the finite element method, the computational domain is decomposed into N_e elements and the element shape functions Φ_i's are introduced. The discretized solution in each element $\Delta\mathbf{q}_h^e(t, x, y)$ can be expressed as

$$\Delta\mathbf{q}_h^e(t, x, y) = \sum_{i=1}^{N_n} \Phi_i(x, y)(\Delta\mathbf{Q}_i(t))^e \tag{41}$$

where N_n is the number of nodes per element and the $(\Delta\mathbf{Q}_i(t))^e$ are the nodal values of $\Delta\mathbf{q}$. The test function $\mathbf{v}$ is chosen as

$$\mathbf{v}(x, y) = \Phi_i(x, y)\mathbf{I} \tag{42}$$

where $\mathbf{I}$ is the identity matrix. Substituting equations (41) and (42) into (40) gives the linear algebraic equation

$$\mathbf{K}^n \Delta\mathbf{Q} = \mathbf{F}^n \tag{43}$$

where $\Delta\mathbf{Q}$ denotes the global nodal values of $\Delta\mathbf{q}(t, x, y)$, and the final global matrix is

$$\mathbf{K}^n = \sum_{e=1}^{N_e} (\mathbf{K}^n)^e \tag{44}$$

That is, the global matrix $\mathbf{K}^n$ is assembled by the element matrix $(\mathbf{K}^n)^e$, which is defined as

$$(\mathbf{K}_{ij}^n)^e = \int_{\Omega_e} (\mathbf{L}\Phi_i)^{\mathrm{T}} \cdot (\mathbf{L}\Phi_j)\, \mathrm{d}\Omega \tag{45}$$

The final right-hand-side vector $\mathbf{F}^n$ is assembled by the element vector $(\mathbf{F}_i^n)^e$, which is given as

$$(\mathbf{F}_i^n)^e = \int_{\Omega_e} (\mathbf{L}\Phi_i)^{\mathrm{T}} \cdot \mathbf{f}\, \mathrm{d}\Omega \tag{46}$$

An important feature of the least-squares finite element method, which can be observed in equations (44) and (45), is that the final global matrix is symmetric. In addition, in the neighbourhood of the solution (that is, if a unique solution exists) the global matrix is also positive-definite. As a result, an iterative method, such as the conjugate gradient method, can be used to effectively invert the matrix. As long as the solution exists, the numerical stability of the iterative solver is guaranteed. However, since this is the first attempt to investigate the low-Mach-number flows by the LSFEM, the formulation and the feasibility of the LSFEM for such flows are of primary concern. Thus, the results in this paper are obtained by a direct solver.

3.3. Weakly imposed conditions

In this work, the equation of state is weakly imposed at every grid node of the computational domain. This weakly imposed treatment is formulated based on the least-squares approach. In other words, we define a global least-squares functional as a combination of the least-squares weak statement for the equation of state and the LSFEM for the differential equations, equation (37), such as

$$\begin{aligned} J_{\bar{\Omega}} &= J_\Omega + I_\Omega \\ &= J_\Omega + \sum_{i=1}^{N_n} [1 + \gamma M^2(\Delta p' + p') - (\rho T + \rho \Delta T + T \Delta \rho)]_i^2 \end{aligned} \tag{47}$$

where J_Ω is the least-squares functional of the differential equations and is defined in equation (37). I_Ω is the least-squares functional for the equation of state. Taking a variational of the functional $J_{\bar{\Omega}}$ with respect to the corresponding variables and minimizing it, we obtain

$$\begin{aligned} \delta J_{\bar{\Omega}} &= \delta J_\Omega + \delta I_\Omega \\ &= \delta J_\Omega + 2 \sum_{i=1}^{N_n} [1 + \gamma M^2(\Delta p' + p') - (\rho T + \rho \Delta T + T \Delta \rho)]_i \\ &\quad \cdot [\gamma M^2 \delta \Delta p' - (\rho \delta \Delta T + T \delta \Delta \rho)]_i \end{aligned} \tag{48}$$

where the original variational statement for the governing equations δJ_Ω is defined in equations (38)–(40). The final weak statement can be expressed as

$$\delta J_{\bar{\Omega}} = \delta J_\Omega + [\alpha_i]\delta I_\Omega = \lfloor 0 \rfloor \tag{49}$$

where $\lfloor 0 \rfloor$ is a null vector and $[\alpha_i]$ is a diagonal matrix with its entries α_i as prescribed coefficients of the corresponding conditions. In practice, large values of α_i are used to enforce the equation of state. This weakly imposed treatment is naturally compatible with the LSFEM employed for solving the transport equations. Alternatively, we could treat the equation of state as part of the governing equations and straightforwardly apply the LSFEM to it. The effect will be the same except that, in this case, the equation of the state is imposed at the Gaussian points of each element instead of the grid nodes. Finally, we like to note that the weakly imposed treatment is also suitable for enforcing complex boundary conditions which otherwise could not be easily implemented.

4. RESULTS AND DISCUSSION

4.1. Lid-driven cavity flow

As shown in Figure 1, the fluid in the cavity is driven by the moving top at a uniform velocity. Since the flow is isothermal, the buoyancy terms in the y-momentum and energy equations are neglected. This problem has been regarded as a benchmark for incompressible flow calculations. Previously, Ghia *et al.*[22] reported detailed results of driven cavity flows at various Reynolds numbers using fine uniform meshes.

In this paper, we calculate this flow by using the compressible formulation to demonstrate the stability of the numerical scheme at the incompressible limit. Four Reynolds numbers, 100, 400, 1000 and 5000, are considered. In all four cases, 25 × 25 bilinear elements clustered near the lid are used. Note that there are two mathematically singular points at the two upper corners of the flow field. Since we use linear elements for the calculations, it is implicitly assumed that the flow

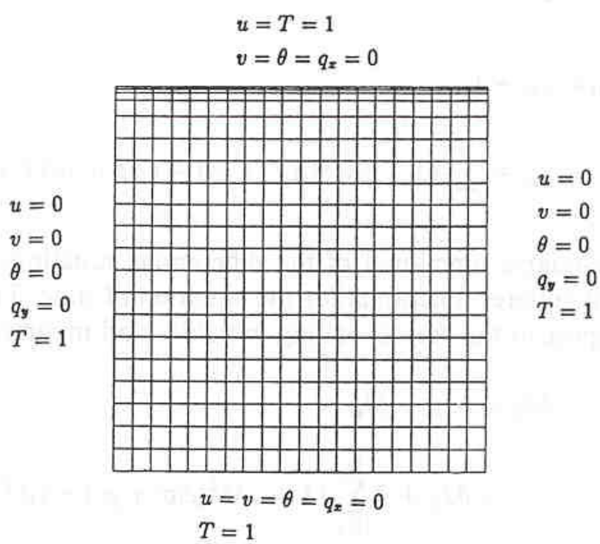

Figure 1. Boundary conditions and computational mesh for the lid-driven cavity flow

properties varied linearly in those two corner elements, i.e. the velocity varies linearly between the no-slip wall and the driving lid in the neighbourhood of the two singular points.

The boundary conditions of the flow field are illustrated in Figure 1, including the no-slip conditions, $u = v = \theta = 0$, and the isothermal conditions $T = 1$, q_x (or q_y) $= 0$. Note that the divergence of velocity is set to be null on the wall ($\theta = 0$). This condition can be derived by imposing $u = v = 0$ to the continuity equation at a steady state.

Figure 2 shows the convergence rates of the four calculations. Within 20 time steps, all four calculations reach machine accuracy. Note that we started the calculation with $Re = 100$ with quiescent fluid as the initial condition. The calculation of $Re = 400$ is based on the solution of $Re = 100$ as the initial condition, and so on. Therefore, the calculation of the $Re = 400$ case reaches the convergence faster than that of the $Re = 100$ case. Velocity vectors of the four cases are shown in Figure 3, in which a large primary vortex near the centre along with secondary recirculations around corners are shown. Figure 4 shows the comparison of the calculated u and v at the vertical and horizontal centrelines with Ghia's data. Favourable agreement is observed.

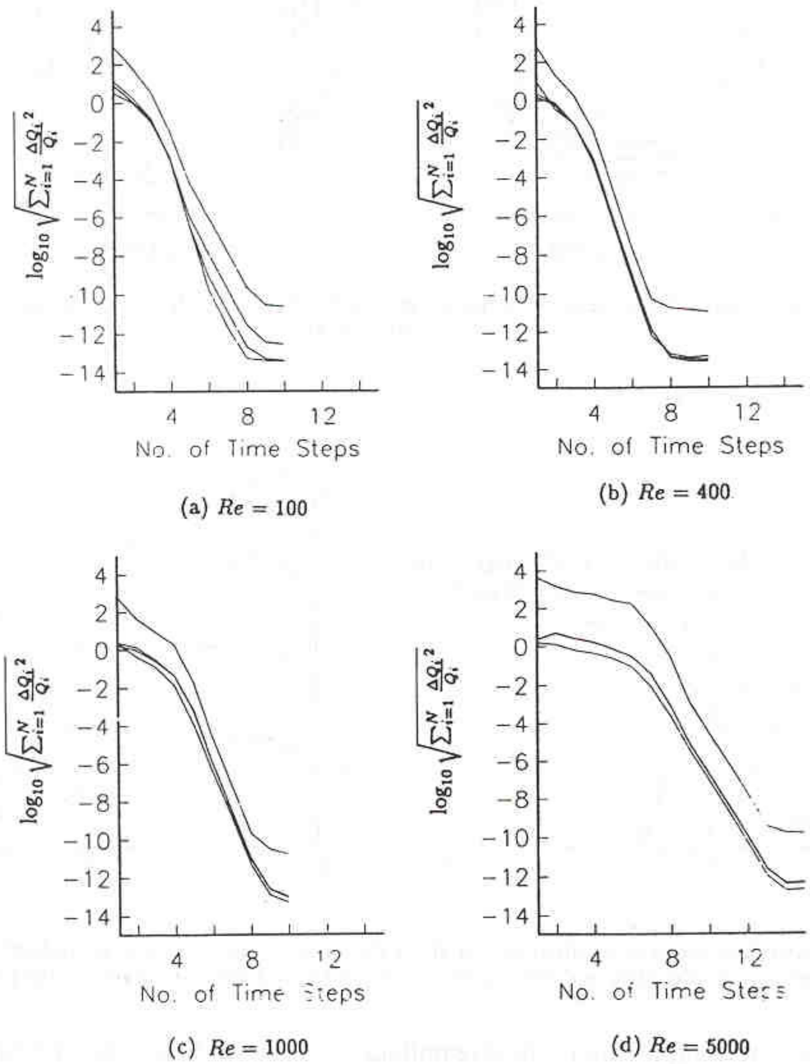

Figure 2. Convergence rates of lid-driven flows in terms of averaged temporal increments of density, temperature and velocities ($Q = \rho, u, v, T$): (a) $Re = 100$, (b) $Re = 400$, (c) $Re = 1000$, (d) $Re = 5000$

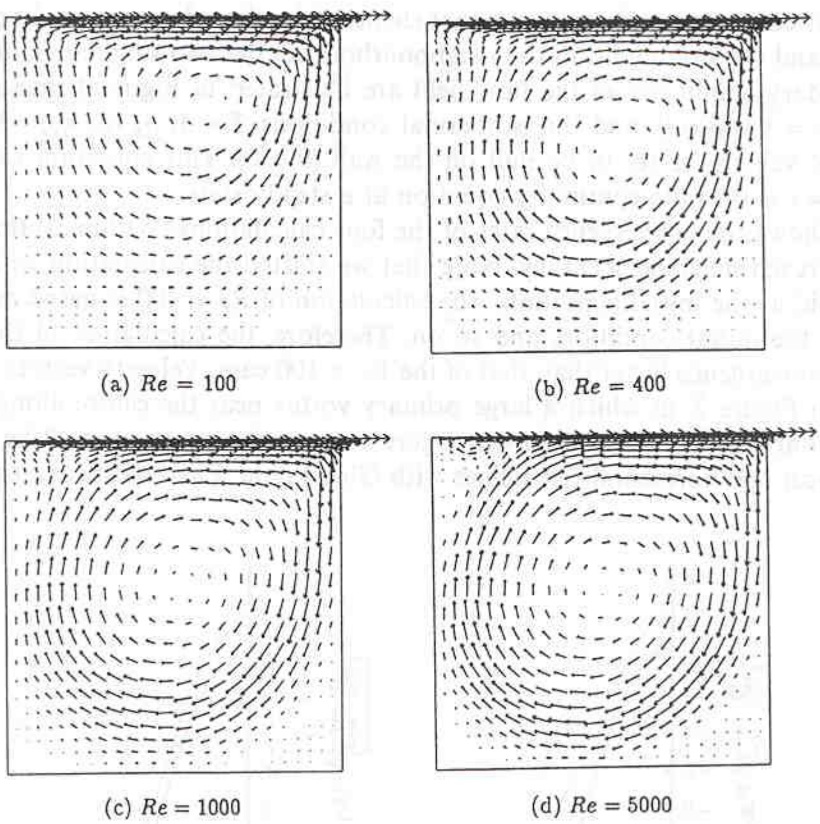

Figure 3. The calculated velocity vectors of lid-driven cavity flows: (a) $Re = 100$, (b) $Re = 400$, (c) $Re = 1000$, (d) $Re = 5000$

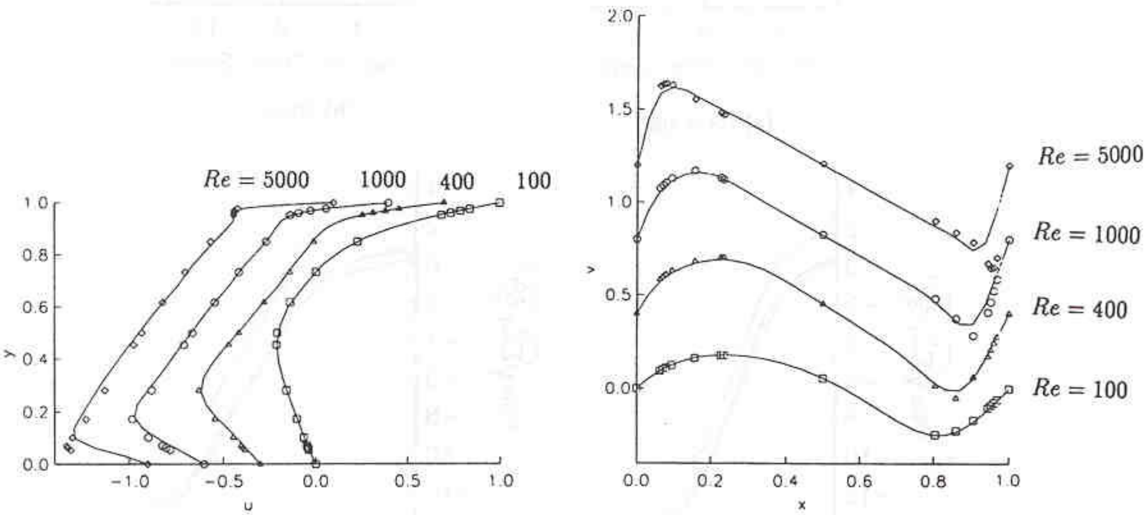

Figure 4. Comparison of the velocity distributions along the vertical and horizontal centrelines with Ghia's data for Reynolds numbers 100, 400, 1000 and 5000 (symbols are Ghia's data and the curves are the present calculations)

Figure 5 shows the comparison of the streamlines of the $Re = 5000$ case with Ghia's result. With very coarse mesh (25×25), the LSFEM catches most of the flow features obtained by Ghia, in which a very fine mesh is used (257×257). This outstanding accuracy of the LSFEM is due to the fact that the order of accuracy of the vorticity (ω), the divergence of the velocity (θ), as well as the

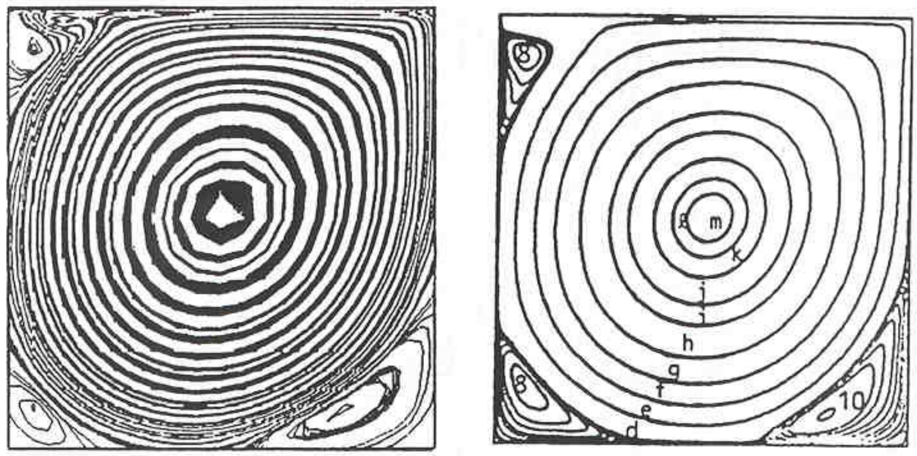

(a) calculated (b) Ghia's

Figure 5. Comparison of the calculated streamlines of driven cavity flow with Ghia's result at $Re = 5000$: (a) calculated, (b) Ghia's

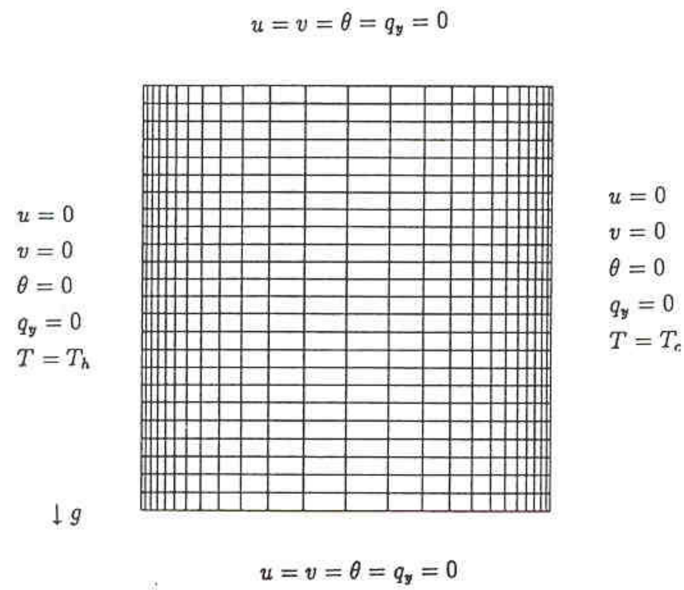

Figure 6. Boundary conditions and computational mesh for the buoyancy-driven flow

heat conduction fluxes ($q_{x,y}$) are the same as that of the primitive flow variables such as velocity and pressure.

4.2. *Buoyancy-driven cavity flow*

The second numerical example is a buoyancy-driven gas flow in a square enclosure. As shown in Figure 6, the configuration consists of two insulated horizontal walls and two vertical walls at different temperatures T_h and T_c. This problem has been extensively studied based on the incompressible flow equations with Boussinesq approximation, which is appropriate only for

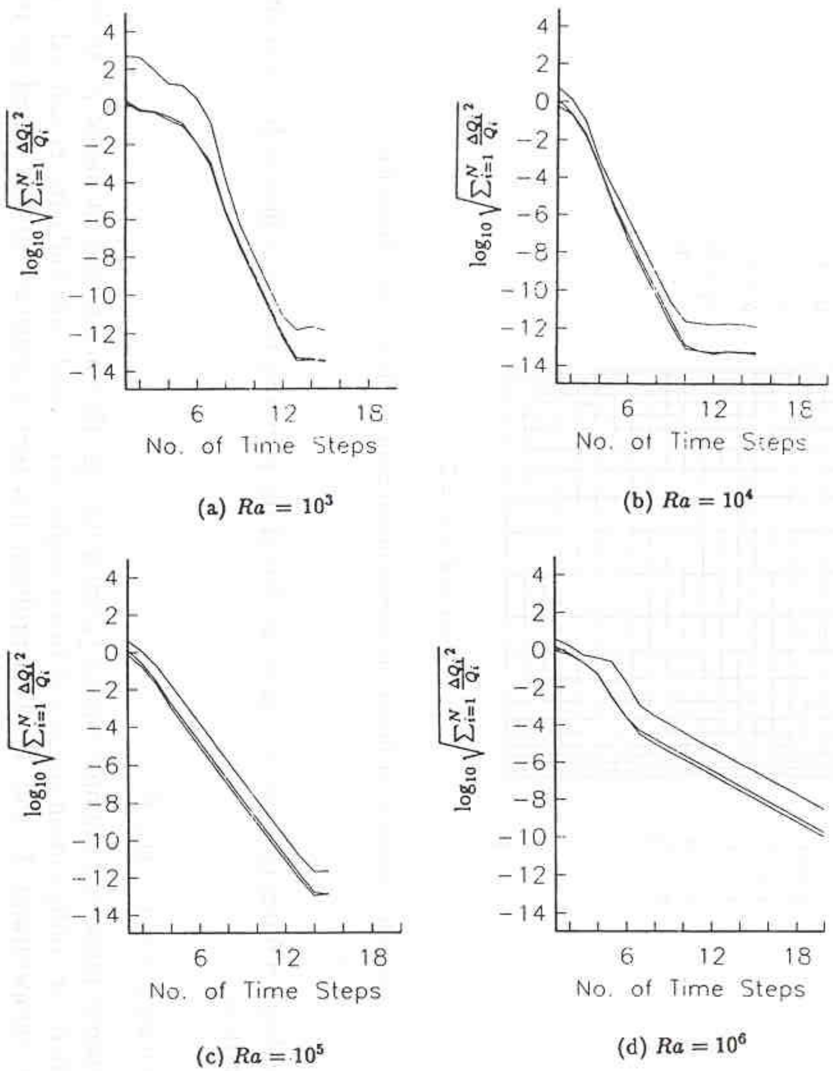

Figure 7. Convergence history of buoyancy-driven flow calculations in terms of averaged temporal increments of density, temperature and velocities ($Q = \rho, u, v, T$): (a) $Ra = 10^3$, (b) $Ra = 10^4$, (c) $Ra = 10^5$, (d) $Ra = 10^6$

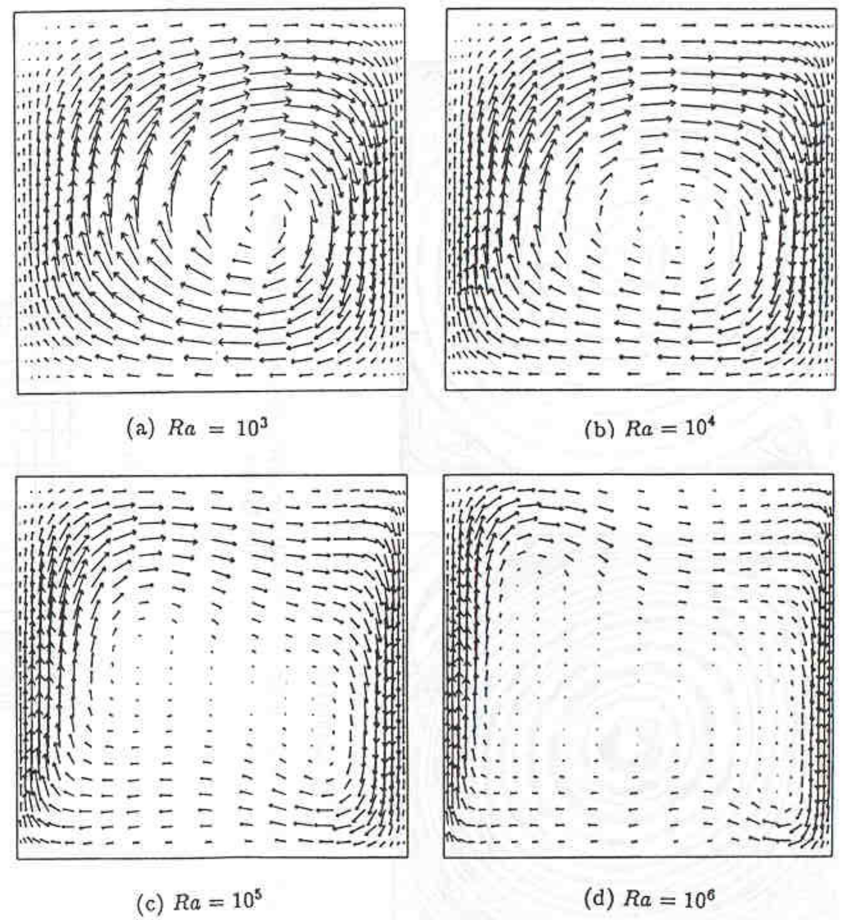

Figure 8. The calculated velocity vectors of buoyancy-driven flows at (a) $Ra = 10^3$, (b) $Ra = 10^4$, (c) $Ra = 10^5$, (d) $Ra = 10^6$

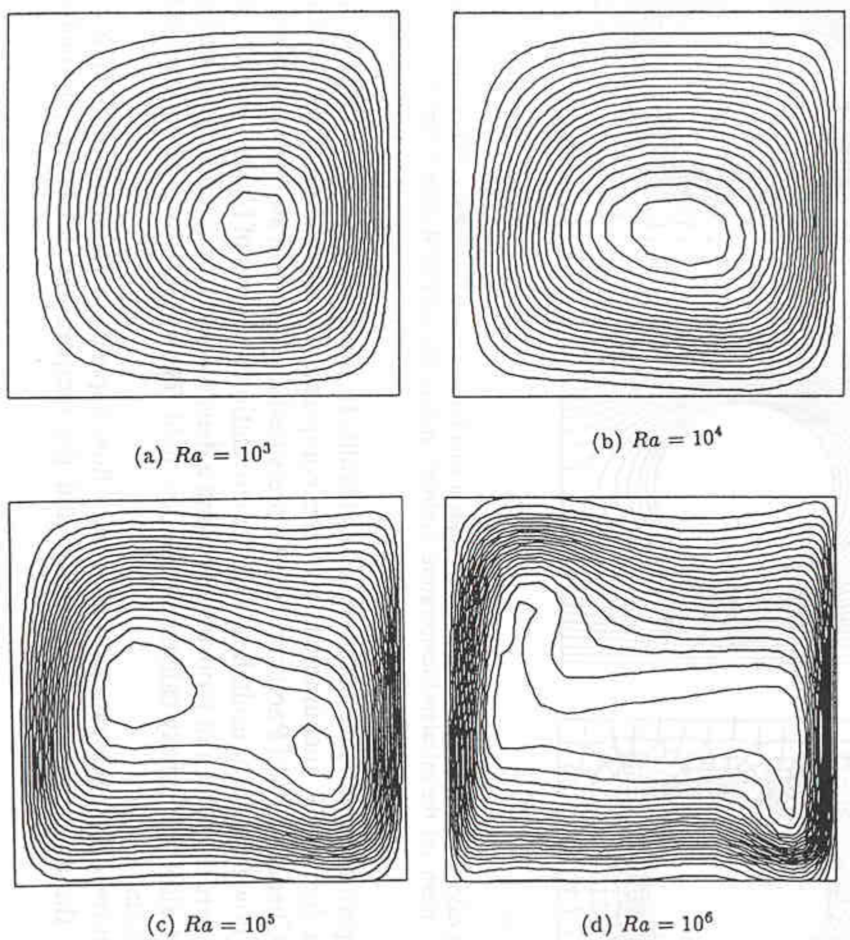

Figure 9. The calculated streamlines of buoyancy-driven flows at (a) $Ra = 10^3$, (b) $Ra = 10^4$, (c) $Ra = 10^5$, (d) $Ra = 10^6$

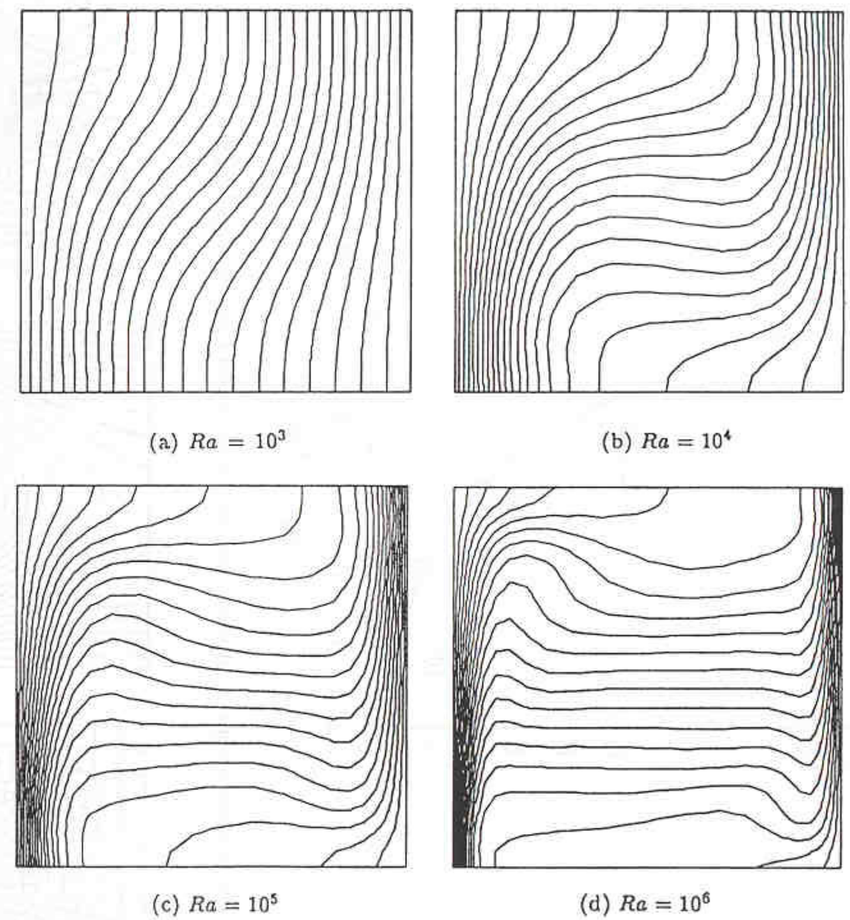

Figure 10. The calculated isothermal contours of buoyancy-driven flows at (a) $Ra = 10^3$, (b) $Ra = 10^4$, (c) $Ra = 10^5$, (d) $Ra = 10^6$

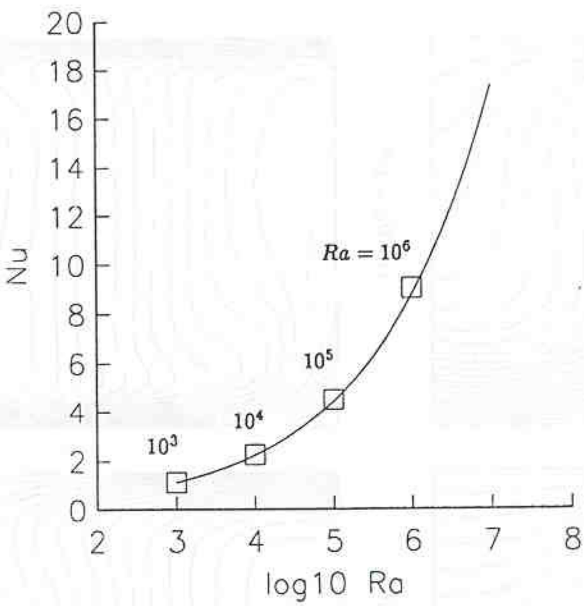

Figure 11. The comparison of the calculated Nusselt numbers with Chenoweth and Paolucci's correlation

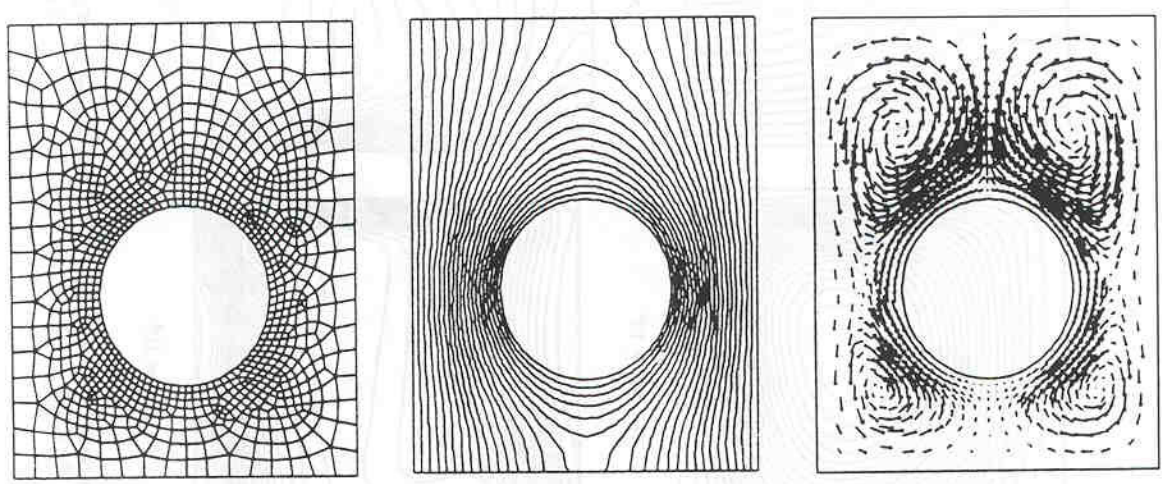

(a) (b) (c)

Figure 12. The calculated solution of a hot cylinder inside a cold box for $\varepsilon = 0{\cdot}2$ and $Ra = 200$: (a) the computational mesh, (b) the calculated temperature contours, and (c) the calculated velocity vectors

a small temperature difference between vertical walls. In practice, however, a large temperature difference is frequently encountered, and the compressible formulation must be employed. Previously, Chenoweth and Paolucci[23] used a pressure-based method and performed an in-depth study of the flow field. As a result, heat transfer correlations in terms of Nusselt number, Rayleigh number, etc., are deduced and reported. By using a density-based, preconditioning method, Choi and Merkle[4] also successfully calculated the flow field. Their results compared favourably with Chenoweth's data.

Flow features of the buoyancy-driven cavity flow depend on Rayleigh number Ra, Froude number Fr, the aspect ratio of the cavity, and the temperature difference parameter ε. For the present study, four Rayleigh numbers, $Ra = 10^3, 10^4, 10^5$ and 10^6, are considered with a temperature difference parameter $\varepsilon = 0{\cdot}6$, which represents $T_h/T_c = 4$. In all four cases, the Froude number and the aspect ratio are unity. A 25×25 mesh clustered near the hot and cold walls is used in all four cases. Figure 7 shows the convergence history of the four calculations. Within 20 steps, all calculations reach machine accuracy.

Figures 8–10 show the velocity vectors, the streamlines and the isothermal contours of the four cases. It is well known that the Boussinesq approximation displays a fully antisymmetric flow field with respect to the centre of the cavity. The present calculation based on the compressible formulation shows an asymmetric flow field which has been observed experimentally. For $Ra = 10^3$ and 10^4, a shift of the vortex centre towards the cold wall is observed. At $Ra = 10^5$ and 10^6, secondary rolls embedded in the primary eddy are observed. The accuracy of the numerical results is verified by comparing the Nusselt number of the convective heat transfer of the whole cavity with a correlation provided by Chenoweth and Paolucci[23] (see Figure 11).

To further demonstrate the capability of the newly developed solver, another buoyancy force driven flow is included. Figure 12 shows a hot cylinder immersed in a box of fluid. The box is composed of two insulated horizontal walls and two vertical walls at a lower temperature. The Rayleigh number is 200 and the temperature difference parameter ε is set at 0·2. As shown in Figure 12(a), about 1000 quadrilateral elements are used. Figure 12(b) shows the temperature contours of the flow field. Figure 12(c) is the velocity vectors, in which four primary recirculations are observed. The calculations converge to machine accuracy in about 25 time steps.

5. CONCLUDING REMARKS

In this paper, we report the development of the LSFEM to simulate low-Mach-number, compressible flows. A ρ–u–v–T–θ–ω–q_x–q_y–p' formulation is proposed for the full compressible flow equations. A suitable non-dimensionalization strategy is developed for the low-Mach-number flows. Two numerical examples were presented: a driven cavity flow at various Reynolds numbers and buoyancy-driven flow at several Rayleigh numbers. Both cases were calculated by using the full compressible formulation. The driven cavity flow poses as an incompressible limit for the compressible flow solver. Nevertheless, the numerical scheme is stable and the calculation reaches machine accuracy within a limited number of time steps. For the driven cavity flows, the simulated result compared favourably with the benchmark data by Ghia. For the buoyancy-driven flow, the compressible flow solver faithfully catches the asymmetric flow features which were observed experimentally but cannot be obtained by employing the incompressible flow equations with the Boussinesq approximation. The accuracy is verified by comparing the calculated Nusselt number with Chenoweth's data. The present result indicates that the LSFEM is a viable method for calculating multi-dimensional, low-Mach-number flows.

REFERENCES

1. S. V. Patankar, *Numerical Heat Transfer and Fluid Flow*, Hemisphere, Washington, DC, 1980.
2. J. T. Oden and G. F. Carey, *Finite Elements, Mathematical Aspects, Vol. IV*, Prentice-Hall, Englewood Cliffs, N.J., 1983.
3. C. L. Merkle and Y.-H. Choi, 'Computation of low-speed compressible flows with time-marching procedures', *Int. j. numer. methods eng.*, **25**, 293–311 (1988).
4. Y. H. Choi and C. L. Merkle, 'The application of preconditioning in viscous flows', *J. Comput. Phys.*, **105**, 207–223 (1993).
5. E. Turkel, 'Review of preconditioning methods for fluid dynamics', *Appl. Numer. Math.*, **12**, 257–284 (1993).

6. A. J. Chorin, 'A numerical method for solving incompressible viscous flow problems', *J. Comput. Phys.*, **2,** 12–26 (1967).
7. E. O. Einset and K. F. Jensen, 'A finite element solution of three-dimensional mixed convection gas flows in horizontal channels using preconditioned iterative matrix methods', *Int. j. numer. methods fluids*, **14,** 817–841 (1992).
8. A. J. Chorin, 'On the convergence of discrete approximations to the Navier–Stokes equations, *Math. Comput.*, **23,** (1969).
9. G. E. Schneider, G. D. Raithby and M. M. Yovanovich, 'Finite element analysis of incompressible fluid flow incorporating equal order pressure and velocity interpolation', in C. Taylor, K. Morgan and C. A. Brebbia (eds.), *Numerical Methods in Laminar and Turbulent Flow*, Pentech Press, Plymouth, 1978.
10. M. Kawahara and K. Ohmiya, 'Finite element analysis of density flow using the velocity correction method', *Int. j. numer. methods fluids*, **5,** 981–993 (1985).
11. G. Comini and S. Del Guidice, 'Finite element solution of the incompressible Navier–Stokes equations', *Numer. Heat Transfer*, **5,** 463–478 (1972).
12. J. G. Rice and R. J. Schnipke, 'An equal-order velocity–pressure formulation that does not exhibit spurious pressure modes', *Comput. Methods Appl. Mech. Eng.*, **58,** 135–149 (1986).
13. O. C. Zienkiewicz and J. Wu, 'Incompressibility without tears—how to avoid restrictions on mixed formulation', *Int. j. numer methods eng.*, **32,** 1189–1203 (1991).
14. B. Ramaswamy and T. C. Jue, 'Recent trends and developments in finite element analysis for incompressible thermal flows', *Int. j. numer. methods eng.*, **35,** 671–708 (1992).
15. T. J. R. Hughes, L. P. Franca and M. Ballestra, 'Circumventing the Babuska–Brezzi conditions, a stable Petrov–Galerkin formulation of the stokes problem accomodating equal-order interpolation', *Comput. Methods Appl. Mech. Eng.*, **59,** 85–99 (1986).
16. P. A. B. Sampaio, 'A Petrov–Galerkin formulation for the incompressible Navier–Stokes equations using equal order interpolations for velocity and pressure', *Int. j. numer. methods eng.*, **31,** 1135–1149 (1991).
17. O. C. Zienkiewicz and J. Wu, 'A general explicit or semi-explicit algorithm for compressible and incompressible flows', *Int. j. numer. methods eng.*, **35,** 457–479 (1992).
18. O. C. Zienkiewicz, J. Wu and J. Peraire, 'A new semi-implicit or explicit algorithm for shallow water equations', *Model. Sci. Comput.*, **1,** 31–49 (1993).
19. B. N. Jiang, T. L. Lin and L. A. Povinelli, 'Large-scale computation of incompressible viscous flow by least-squares finite element method', *Comput. Methods Appl. Mech. Eng.*, to appear.
20. B. N. Jiang and L. A. Povinelli, 'Optimal least-squares finite element method for elliptic problems', *Comput. Methods Appl. Mech. Eng.*, **102,** 199–212 (1993).
21. B. N. Jiang and L. A. Povinelli, 'Least-squares finite element method for fluid dynamics', *Comput. Methods Appl. Mech. Eng.*, **81,** 13–37 (1990).
22. U. Ghia, K. N. Ghia and C. T. Shin, 'High-*Re* solutions for incompressible flow using the Navier–Stokes equations and a multigrid method', *J. Comput. Phys.*, **48,** 387–411 (1982).
23. D. R. Chenoweth and S. Paolucci, 'Natural convection in an enclosed vertical air layer with large horizontal temperature differences', *J. Fluid Mech.*, **169,** 173–210 (1986).
24. D. L. Lefebvre, J. Peraire and K. Morgan, 'Least squares finite element solution of compressible and incompressible flows', *Int. J. Numer. Methods Heat Transfer*, **2,** 99–113 (1992).
25. D. L. Lefebvre, J. Peraire and K. Morgan, 'Finite element least squares solution of the Euler equations using linear and quadratic approximations', *Comput. Fluid Dyn.*, **1,** 1–23 (1993).
26. M. Hafez, M. Soliman and S. White, 'A unified approach for numerical solution of viscous compressible and incompressible flows over adiabatic and isothermal walls', 5th Symp. on Numerical and Physical Aspects of Aerodynamic Flows, California State University, Long Beach, California, 1992.